

# Anisotropic Galactic Outflows and Enrichment of the Intergalactic Medium. I: Monte Carlo Simulations

Matthew Pieri<sup>1</sup>, Hugo Martel<sup>1</sup>, and Cédric Grenon<sup>1,2</sup>

## ABSTRACT

We have designed an analytical model to describe the evolution of anisotropic galactic outflows. With this we investigate the impact of varying opening angle on galaxy formation and the evolution of the intergalactic medium. We have implemented this model in a Monte Carlo algorithm to simulate galaxy formation and outflows in a cosmological context. Using this algorithm, we have simulated the evolution of a comoving volume of size  $(12h^{-1}\text{Mpc})^3$  in the  $\Lambda\text{CDM}$  universe. Starting from a Gaussian density field at redshift  $z = 24$ , we follow the formation of  $\sim 20,000$  galaxies, and simulate the galactic outflows produced by these galaxies. When these outflows collide with density peaks, 80% of the time this results in ram pressure stripping of the gas inside the peak, preventing the formation of a galaxy. Anisotropic outflows follow the path of least resistance, and thus travel preferentially into low-density regions, away from cosmological structures (filaments and pancakes) where galaxies form. As a result, the number of collisions is reduced, leading to the formation of a larger number of galaxies. Anisotropic outflows can significantly enrich low-density systems with metals. Conversely, the cross-pollution in metals of objects located in a common cosmological structure, like a filament, is significantly reduced. Highly anisotropic outflows can travel across cosmological voids, and deposit metals in other, unrelated cosmological structures.

*Subject headings:* cosmology — galaxies: formation — intergalactic medium — methods: analytical

## 1. INTRODUCTION

### 1.1. Anisotropic Outflows

Galactic outflows play an important role in the evolution of galaxies and the intergalactic medium (IGM). Supernova explosions in galaxies create galactic winds, which deposit energy and metal-enriched gas into the IGM. These outflows are necessary to explain many observations and to solve many problems in galaxy formation, such as the high mass-to-light ratio of dwarf galaxies, the observed metallicity of the IGM, the entropy content of the IGM, the abundance of dwarf galaxies in the Local Group, the overcooling problem, and the angular momentum problem, amongst others.

High-resolution, gasdynamical simulations of explosions in a single object reveal that outflows generated by such explosions tend to be highly anisotropic, with the energy and metal-enriched gas being channeled along the direction of least resistance, where the pressure is the lowest (Mac Low & Ferrara 1999; Martel & Shapiro 2001a,b). Furthermore, several observations support the existence of anisotropic outflows (e.g.

---

<sup>1</sup>Département de physique, génie physique et optique, Université Laval, Québec, QC, G1K 7P4, Canada

<sup>2</sup>Hubert Reeves fellow

Bland & Tully 1988; Fabbiano, Heckman, & Keel 1990; Carignan et al. 1998; Shopbell & Bland-Hawthorn 1998; Strickland et al. 2000; Veilleux & Rupke 2002).

Indirect support for the existence of anisotropic outflows comes from the observed enrichment of systems around the mean density of the universe (Schaye et al. 2003; Pieri & Haehnelt 2004) and the enrichment of systems far from known galaxies at  $z \sim 3$  (Pieri, Schaye, & Aguirre 2006). It may be challenging to enrich such regions with isotropic outflows even with the inclusion of enrichment from poorly understood Population III stars and early indications are that these objects are unlikely to pollute the IGM to a large extent (Norman, O’Shea, & Paschos 2004). Anisotropic outflows may also provide an explanation for part of the observed scatter in the metallicity in the IGM which is still unexplained (Pieri, Schaye, & Aguirre 2006).

Several simulations of galactic outflows in cosmological contexts have been performed. Typically, these simulations use cubic comoving volumes of size  $\sim (10 \text{ Mpc})^3$ , containing thousands of galaxies. Anisotropic outflows have not been considered fully in these simulations.

The methods used can be divided into two groups: analytical methods and numerical methods. The analytical methods are essentially Monte Carlo simulations. Outflows are represented using an analytical solution (e.g. Scannapieco & Broadhurst 2001, hereafter SB01) and currently assume isotropy. The formation of galaxies is calculated using a Gaussian random realization of an initial density field, combined with a spherical collapse model to estimate the collapse redshift and virial temperature, and a model for radiative cooling. The numerical simulations use hydrodynamical algorithms such as SPH, and outflows are generated by imparting a large velocity component to SPH particles (e.g. Aguirre et al. 2001; Scannapieco, Thacker, & Davis 2001; Springel & Hernquist 2003; Oppenheimer & Davé 2006) or depositing additional thermal energy in SPH particles (e.g. Theuns et al. 2002). In these simulations, the outflows themselves are simulated numerically, but the resolution of the simulations are often too poor to describe the dense regions where the anisotropy is generated. While these simulations include some anisotropic behavior they do not investigate its contribution and its severity.

To overcome these limitations, and study anisotropic outflows in a cosmological context, we need an analytical model for the outflows, that could then be combined with either a analytical method or a semi-analytic method for the description of galaxy formation. In this paper, we use a analytical Monte Carlo method. Calculations performed with an N-body semi-analytic approach will be presented in a forthcoming paper (Martel, Grenon, & Pieri 2006).

This paper is set out as follows. In §2, we describe our analytical model for anisotropic outflows. In §3, we describe our Monte Carlo method for cosmological simulations. Results are presented in §4, and their implications are discussed in §5. Conclusions are presented in §6.

## 2. A MODEL FOR ANISOTROPIC OUTFLOWS

Consider a density field with a local density maximum at some position,  $P$ . A halo will collapse at that point, forming a galaxy which will then produce an outflow. Our goal is to design an analytical model for the geometry and evolution of this outflow, that takes into account the physical properties of the galaxy, the density distribution of the matter surrounding the galaxy, and the global properties of the IGM.

Using the high-resolution simulations and the observations of galactic outflows as a guide, we will represent outflows as “bipolar spherical cones.” In a spherical coordinate system  $(r, \theta, \phi)$ , the outflow occupies

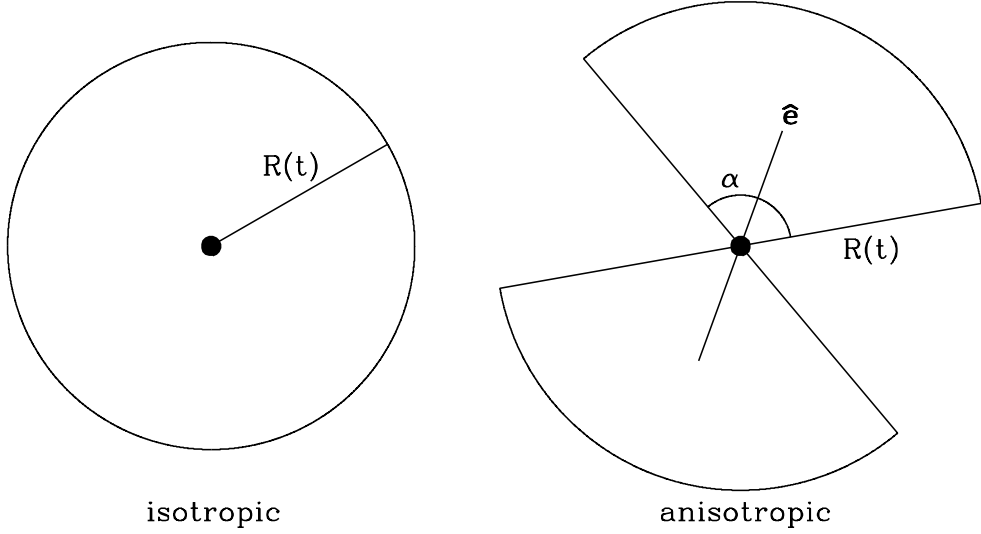


Fig. 1.— Geometry of the isotropic and anisotropic outflows. The isotropic outflows are spherical; the anisotropic ones are bipolar spherical cones.  $R(t)$  is the time-dependent radius of the outflow,  $\alpha$  is the opening angle, and  $\hat{\mathbf{e}}$  the direction of the outflow.

the volume defined by  $r \leq R(t)$ ,  $\theta \leq \alpha/2$  or  $\theta \geq \pi - \alpha/2$ , and  $0 \leq \phi < 2\pi$  where  $R(t)$  is the radius of the outflow and  $\alpha$  is the opening angle. This is illustrated in Figure 1.

In the limit  $\alpha = \pi$ , the outflow becomes spherical, and is entirely described by the radius,  $R(t)$ . If  $\alpha < \pi$ , the outflow is anisotropic, and two additional parameters must be specified: the opening angle  $\alpha$ , and the direction of the outflow, which is defined by a unit vector  $\hat{\mathbf{e}}$ . Hence, our model of anisotropic outflows is a 3-parameter model.

## 2.1. The Opening Angle

It is not clear what value one should be using for the opening angle. The simulations of Mac Low & Ferrara (1999) and Martel & Shapiro (2001a) show that the angle actually varies as the expansion proceeds. It starts at a low value,  $\alpha \sim 10^\circ - 45^\circ$  near the site of the explosion. Once the outflow reaches the low-density regions, it “fans out,” and the opening angle increases to values  $\alpha \sim 45^\circ - 100^\circ$ , or even larger. The radius also varies with opening angle. Hence, our representation of outflows as bipolar spherical cones is a convenient simplification. Until we have a better understanding of the morphology of the outflows (something that would require more precise simulations), we will treat the opening angle as a free parameter that can take any value from  $\alpha = 180^\circ$  (the isotropic limit) to  $\alpha \sim 20^\circ$  (the jets limit), keeping in mind that the larger values are likely to provide a more accurate description of the outflows once they reach the low-density regions.

## 2.2. The Direction of the Outflow

The outflows are expected to take a path of least resistance out of a galaxy that forms at the location of a density peak. In the current literature, two characteristic scales for this path of least resistance have been considered: the galactic scale in which a disk may form (Mac Low & Ferrara 1999), and larger scale filamentary or pancake structures (Martel & Shapiro 2001a,b). In the former case, outflows are directed along the rotation axis of the galaxy. In the latter the pressure of the surrounding medium determines the direction of the outflow. We have selected the latter as the defining scale upon which our anisotropic outflows are based, for the following reasons:

- It is unclear if the galaxy has already formed a well-ordered disk by the time much of the initial starburst has occurred. Outflows may start while the galaxy is still in the process of assembling. Hydrodynamical simulations of galaxy formations suggest that starbursts take place during a chaotic merger events at high redshift, before a disk has assembled (Brook et al. 2005, 2006).
- Despite recent results suggesting their rotation axes tend to lie preferentially parallel to the plane of pancake structures (Noh & Lee 2006, and references therein) the orientation of these disks are largely randomized. Averaging over all outflowing galaxies, only a weak directionality is expected before the effect of larger scale structures begins to dominate as the outflows continue to expand.
- The importance of disk-scale effects is dependent on the locations of SNe within the disk. Off-center SNe in a disk will not result in outflows that are directed parallel to the spin axis since the relative pressure gradient does not favor this direction to the same extent.

Figure 2 shows an intermediate stage of a simulation by Martel & Shapiro (2001a) of an explosion inside a dwarf galaxy that is forming at the intersection of two emerging filaments inside a cosmological pancake. This simulation was performed with an Adaptive SPH algorithm (Shapiro et al. 1996; Owen et al. 1998) with  $64^3$  gas and  $64^3$  dark-matter particles. The outflow is clearly anisotropic, bipolar, and propagates in the direction normal to the pancake plane. Interestingly, the central region where the explosion takes place has a nearly isotropic density profile. Hence, it is the anisotropy of the outer regions that results in an anisotropic outflow.

In our Monte Carlo simulations, we assume that galaxies form at the location of local density peaks in the matter distribution, and we determine the direction of the outflow by finding the direction of least resistance in the vicinity of that peak. We discuss in greater detail the concepts of “peaks” and “vicinity” in §§3.2 and 3.3 below.

Consider a local density maximum located at some point,  $P$ , inside the computational volume. We center a cartesian coordinate system  $(x, y, z)$  on that point, and perform a Taylor expansion of the density contrast up to second order,

$$\delta(x, y, z) = \delta_{\text{peak}} - Ax^2 - By^2 - Cz^2 - 2Dxy - 2Exz - 2Fyz. \quad (1)$$

This expression contains no linear terms since the density is a local maximum. In practice, we consider the density distribution inside a sphere of radius,  $R^*$ , centered on the point,  $P$ , and perform a least-square fit of equation (1) to determine numerically the values of the 6 coefficients  $A, B, C, D, E, F$ . Once these coefficients are determined, we rotate of the coordinate system, such that in the new coordinate system

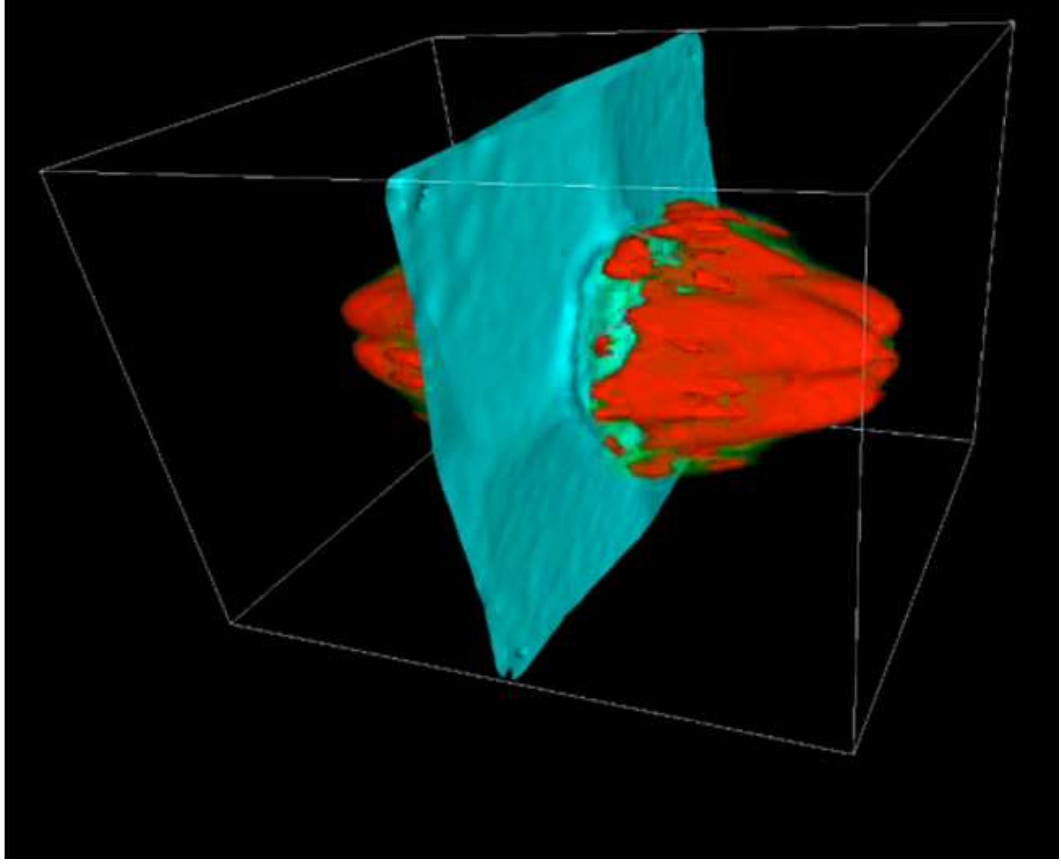


Fig. 2.— Snapshot of a hydrodynamical simulation of an explosion inside a cosmological pancake. Blue: density isosurface, showing the pancake. Notice the circular ripple resulting from the explosion. Red: temperature isosurface, showing the outflow.

$(x', y', z')$  the cross-terms vanish. Equation (1) reduces to

$$\delta(x', y', z') = \delta_{\text{peak}} - A'x'^2 - B'y'^2 - C'z'^2. \quad (2)$$

It is actually straightforward to perform this change of coordinates. We combine the coefficients of equation (1) to form the following matrix,

$$M = \begin{bmatrix} A & D & E \\ D & B & F \\ E & F & C \end{bmatrix}. \quad (3)$$

We then diagonalize this matrix. Since this matrix is real and symmetric, all three eigenvalues are real. These eigenvalues are the coefficients  $A'$ ,  $B'$ ,  $C'$ , respectively, and the 3 corresponding eigenvectors give us the directions of the three coordinate axes  $x'$ ,  $y'$ , and  $z'$ , respectively.

The three coefficients  $A'$ ,  $B'$ , and  $C'$  are always positive, otherwise the point,  $P$ , would not be a maximum, but rather a saddle point or a minimum. Each coefficient is a measure of how fast the density drops as we move away from the peak in the direction corresponding to that coefficient. Therefore, the

largest coefficient corresponds to the direction along which the density drops the fastest. We will interpret this as being the direction of least resistance, and assume that the outflow will naturally follow that direction. For instance, if  $B'$  happens to be the largest of the 3 coefficients, then the outflow will be directed along the  $y'$ -axis.

### 2.3. The Expansion of the Outflow

In this section, we present the equations describing the expansion of the outflow. The technique used for solving these equations is presented in Appendix A.

#### 2.3.1. Basic Equations

The expansion of isotropic outflows in an expanding universe was originally described by Tegmark, Silk, & Evrard (1993, hereafter TSE). The injection of energy produces an outflow of radius,  $R$ , which consists of a dense shell containing a cavity. A fraction,  $1 - f_m$ , of the gas is piled up in the shell, while a fraction,  $f_m$ , of the gas is distributed inside the cavity. We normally assume  $f_m \ll 1$ , that is, most of the gas is located inside the shell and this is called the *thin-shell approximation*.

The original equations of TSE have been refined by several authors (Madau, Ferrara, & Rees 2001; SB01; Scannapieco, Ferrara, & Madau 2002, hereafter SFM) to include various additional physical processes. Hence, there is not a “unique” form of the equations. In this paper, the evolution of the shell radius,  $R$ , is described by the following system of equations,

$$\ddot{R} = \frac{8\pi G(p - p_{\text{ext}})}{\Omega_b H^2 R} - \frac{3}{R}(\dot{R} - HR)^2 - \frac{\Omega H^2 R}{2} - \frac{GM}{R^2}, \quad (4)$$

$$\dot{p} = \frac{L}{2\pi R^3} - \frac{5\dot{R}p}{R}, \quad (5)$$

where a dot represents a time derivative,  $\Omega$ ,  $\Omega_b$ , and  $H$  are the total density parameter, baryon density parameter, and Hubble parameter at time,  $t$ , respectively,  $L$  is the luminosity (discussed in §2.3.3),  $p$  is the bubble pressure resulting from this luminosity, and  $p_{\text{ext}}$  is the external pressure of the IGM. These expressions most closely resemble that of SFM, the one difference coming from their use of a radially dependent mass in the last term of equation (4), derived by assuming a NFW profile (Navarro, Frenk, & White 1997). This is motivated by the gravitational drag on a spherical outflow expanding out of a spherical collapsed halo, and is no longer an adequate description in the case being examined since an anisotropic outflow will more rapidly escape an elliptical halo. The influence of the gravitational potential well will be an intermediate case between this and a point mass. In practice we take the simpler form by assuming a point mass, as in SB01. We found, a posteriori, that the vast majority of outflows will reach a radius that significantly exceeds the size of the halo from which they originate. Hence, the details of the halo density profile are not crucial.

To describe anisotropic outflows, we need to modify these equations. First consider equation (5). The two terms in the right hand side correspond to the increase in pressure caused by energy injection, and the decrease in pressure caused by the expansion of the outflow, respectively. At this point, we need to backtrack. Equation (5) was derived from the following system of equations (TSE):

$$E_t = \frac{3pV}{2}, \quad (6)$$

$$\dot{E}_t = L - p\dot{V}, \quad (7)$$

where  $E_t$  is the thermal energy inside the outflow, and  $V$  is the volume of the outflow. We take the time derivative of equation (6), and eliminate  $\dot{E}_t$  using equation (7). We get

$$\dot{p} = \frac{2L}{3V} - \frac{5p\dot{V}}{3V}. \quad (8)$$

If we now substitute  $V = 4\pi R^3/3$ , we recover equation (5). However, a bipolar anisotropic outflow with opening angle,  $\alpha$ , has a volume given by

$$V = \frac{4\pi R^3}{3} \left(1 - \cos \frac{\alpha}{2}\right). \quad (9)$$

We substitute equation (9) in equation (8), and get

$$\dot{p} = \frac{L}{2\pi R^3[1 - \cos(\alpha/2)]} - \frac{5\dot{R}p}{R}. \quad (10)$$

Physically, as  $\alpha$  decreases, the energy is injected in a smaller volume, resulting in a larger pressure,  $p$ . This equation replaces equation (5). In our model, this is the only modification we need to make to the equations describing the expansion of the outflow (although a modification to the luminosity will be required). Equation (4) remains unchanged.

### 2.3.2. The External Pressure

The external pressure,  $p_{\text{ext}}$ , depends upon the density and temperature of the IGM, which can be quite complex. But in the context of the analytic approximation we are using, we are justified in making some simplifying approximations. Following Madau, Ferrara, & Rees (2001), we will assume a photoheated IGM with a fixed temperature,  $T_{\text{IGM}} = 10^4 \text{ K}$ . We will also assume an IGM density,  $\rho_{\text{IGM}}$ , equal to the mean baryon density,  $\bar{\rho}_b$ . Hui & Gnedin (1997) performed detailed hydrodynamical calculations of the equation of state for a photoheated IGM, and showed that the temperature is a function of the density. But according to their Figure 1, a temperature of  $10^4 \text{ K}$  is appropriate for densities,  $\rho \approx \bar{\rho}_b$ . The external pressure is then given by

$$p_{\text{ext}}(z) = \frac{\bar{\rho}_b k T_{\text{IGM}}}{\mu} = \frac{3\Omega_{b,0} H_0^2 k T_{\text{IGM}} (1+z)^3}{8\pi G \mu}, \quad (11)$$

where  $z$  is the redshift,  $\mu$  is the mean molecular mass, and subscripts 0 indicate present values. The value of  $\mu$  depends upon the ionization state of the gas. Choudhury & Ferrara (2005, 2006) find that the hydrogen and helium in the IGM are singly-ionized for most of the redshift range in which our outflows are actively expanding. We will assume that this is the case throughout the simulations.

The situation inside the outflow is even more uncertain. The ionization state might even be a function of distance from the source. Until we have a more precise model for the internal structure of the outflow, we will simply make the same assumption as for the surrounding IGM: ionized hydrogen and singly-ionized helium. Notice that this is consistent with TSE, who implicitly assume  $n_e = n_{\text{ion}}$  in their calculation of the Compton luminosity. The mean molecular weight is then  $\mu = 2/(4 - 3Y)$  a.m.u. (atomic mass units). For a helium abundance,  $Y = 0.242$  (Izotov & Thuan 2004), we get  $\mu = 0.611$  a.m.u..

### 2.3.3. The Luminosity

The luminosity,  $L$ , is the rate of energy deposition or dissipation within the outflow and is a sum of five terms,

$$L(t) = L_{\text{SN}} - L_{\text{comp}} - L_{\text{ne}^2} - L_{\text{ion}} + L_{\text{diss}}, \quad (12)$$

where  $L_{\text{SN}}$  is the total luminosity of the supernovae responsible for generating the outflow,  $L_{\text{comp}}$  represents the cooling due to Compton drag against CMB photons,  $L_{\text{ne}^2}$  represents the cooling due to 2-body interactions,  $L_{\text{ion}}$  represents the cooling due to ionization, and  $L_{\text{diss}}$  represents heating from collisions between the shell and the IGM. Following SFM, we will assume that the first two terms, supernovae and Compton drag, dominate, and will neglect the remaining terms. The supernovae luminosity, for a galaxy of mass,  $M$ , is given by

$$L_{\text{SN}} = \frac{f_w E_0}{t_{\text{burst}}} \frac{M_*}{M_{\text{req}}} = 2.86 f_w f_* \left( \frac{\Omega_{b,0}}{\Omega_0} \right) \left( \frac{M}{1M_{\odot}} \right) L_{\odot}, \quad (13)$$

where  $f_w$  is the fraction of the total energy released that goes into the outflow,  $f_*$  is the star formation efficiency, and the total mass in stars formed during the starburst is  $M_* = f_* M \Omega_{b,0} / \Omega_0$ .  $M_{\text{req}}$  is the mass of stars required to form one SN and we take a value of  $M_{\text{req}} = 89.7M_{\odot}$  (derived using a broken power-law IMF from Kroupa 2001) and the energy released by each of these SNe is  $E_0 = 10^{51} \text{ ergs s}^{-1}$ . Leitherer & Heckman (1995) show that for instantaneous star formation, as considered here, the SN outflow phase associated with this burst last for a duration of  $t_{\text{burst}} = 5 \times 10^7 \text{ yr}$  and the delay before the first SNe is negligible. We use the galaxy mass dependent determination of  $f_w$  given by SFM.

Following TSE, the Compton luminosity is given by

$$L_{\text{comp}} = \frac{\pi^2}{15} (\sigma_t c n_e) \left( \frac{k T_e}{m_e c^2} \right) (k T_{\gamma})^4 \frac{V}{(\hbar c)^3}, \quad (14)$$

where  $\sigma_t = 8\pi r_0^2/3 = 8\pi e^4/3m_e^2 c^4$  is the Thompson cross section,  $T_{\gamma}$  is the CMB temperature, and  $n_e$  and  $T_e$  are the electron number density and temperature inside the bubble, respectively. The pressure,  $p$ , inside the bubble is given by

$$p = n k T_e = (n_e + n_{\text{ion}}) k T_e V. \quad (15)$$

We assume that hydrogen is ionized and helium is singly-ionized and hence  $n_{\text{ion}} = n_e$ , which is also the approximation made in TSE. Equation (15) becomes  $n_e k T_e = p/2$ . We now eliminate  $n_e k T_e$  in equation (14). We also eliminate  $V$  using equation (9), and get

$$L_{\text{comp}} = \frac{2\pi^3}{45} \frac{\sigma_t \hbar}{m_e} \left( \frac{k T_{\gamma 0}}{\hbar c} \right)^4 \left( 1 - \cos \frac{\alpha}{2} \right) (1+z)^4 p R^3, \quad (16)$$

where  $T_{\gamma 0}$  is the present CMB temperature. We used  $T_{\gamma} = T_{\gamma 0}(1+z)$ , which is valid over the range of redshifts we consider.

### 2.3.4. The Final Stage of the Outflow

The expansion of the outflow is initially driven by the supernovae luminosity. After the supernovae turn off, the outflow enters the “snowplow phase.” The pressure inside the outflow keeps driving the expansion,

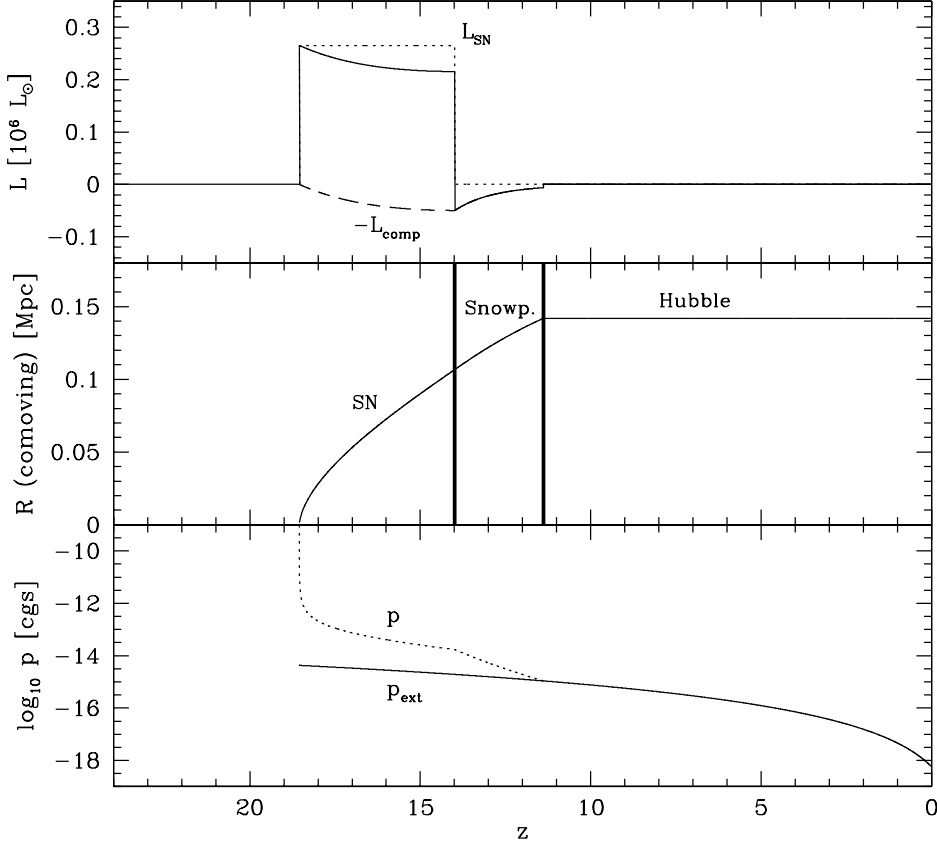


Fig. 3.— Evolution of a particular outflow. The middle panel shows the comoving radius of the outflow versus redshift,  $z$ . The thick lines separate the various phases of the expansion (supernova-driven, snowplow, Hubble expansion). The top panel shows the supernova luminosity,  $L_{\text{SN}}$  (dotted line), Compton luminosity,  $L_{\text{comp}}$  (dashed line), and total luminosity,  $L = L_{\text{SN}} - L_{\text{comp}}$  (solid line), versus redshift. The bottom panel shows the external IGM pressure (solid line) and the pressure of the outflow (dotted line).

but this pressure drops rapidly since there is no energy input from supernovae. Eventually, the pressure will drop down to the level of the external IGM pressure. At that point, the expansion of the outflow will simply follow Hubble expansion. Since we assume identical mean molecular weights inside and outside the outflow, the condition  $p = p_{\text{ext}}$  implies  $T = T_{\text{IGM}} = 10^4 \text{ K}$ .

Figure 3 shows the isotropic outflow solution for a halo of mass,  $M = 7.61 \times 10^7 M_{\odot}$ , which collapses at redshift,  $z = 18.55$ , in a  $\Lambda$ CDM universe. The cooling time is very short, 28,000 years, so the outflow turns on essentially at the same redshift. The top panel shows the total luminosity and the contribution from both the heating by SNe and cooling by Compton drag,  $L_{\text{comp}}$ , the middle panel shows the comoving radius, and the bottom panel shows the pressure,  $p$ , of the outflow and the external pressure,  $p_{\text{ext}}$ , of the IGM. Initially, during the supernova phase, the outflow is driven by the energy input from supernovae and the radius steadily increases. During this phase, the supernova luminosity,  $L_{\text{SN}}$ , exceeds the Compton luminosity by factors of several (at least for this particular outflow). The pressure is infinite at the redshift of supernova

turn-on, but then drops as  $t^{-4/5}$  (see Appendix A). At  $z = 13.99$ , the supernovae burn out, and the only contribution to the total luminosity is the energy loss by Compton drag. The outflow enters the snowplow phase. The turn-off of the supernovae produces a change of slope in the pressure, which in turns produces a change of slope in the Compton luminosity. The snowplow phase lasts until redshift  $z = 11.39$ . At that point, the pressure of the outflow becomes equal to the external pressure, and the outflow switches to pure Hubble expansion.

### 3. THE MONTE CARLO METHOD

We use essentially the same Monte Carlo method as in SB01, generalized to include anisotropic outflows. In our dynamical equation for the evolution of the outflow [eq. (4)], we include the external pressure,  $p_{\text{ext}}$ , an effect that was neglected by SB01, but included by SFM.

#### 3.1. Cosmological Model and Initial Conditions

We consider a  $\Lambda$ CDM model with present density parameter,  $\Omega_0 = 0.27$ , baryon density parameter,  $\Omega_{b,0} = 0.04444$ , cosmological constant,  $\lambda_0 = 0.73$ , Hubble constant,  $H_0 = 71 \text{ km s}^{-1} \text{Mpc}^{-1}$  ( $h = 0.71$ ), primordial tilt,  $n_s = 0.93$ , and CMB temperature,  $T_{\text{CMB}} = 2.725$ , consistent with the results of WMAP (Bennett et al. 2003). We simulate structure formation inside a comoving cubic volume of size,  $L_{\text{box}} = 12h^{-1}\text{Mpc}$ , with periodic boundary conditions. To generate initial conditions, we lay down a cubic grid of size  $512 \times 512 \times 512$  in the computational volume, and compute the initial density contrast,  $\delta_i$ , at initial redshift,  $z_i = 24$ . We also compute, on 10 similar grids, the same density contrast, but filtered at the 10 mass scales:  $M_1, M_2, \dots, M_{10}$ . As we use a Gaussian filter, the mass,  $M$ , and comoving radius,  $R_f$ , of the filter are related by  $M = (2\pi)^{3/2} R_f^3 \bar{\rho}_0$ , where  $\bar{\rho}_0 = 3\Omega_0 H_0^2 / 8\pi G$  is the present mean density of the universe. The values of the mass and length filtering scales are listed in Table 1. The last two columns indicate the filtering radius in units of the grid spacing,  $\Delta$ , and in units of the box size,  $L_{\text{box}}$ .

The method for generating these 11 grids is described in great detail by Martel (2005). Essentially, we work in  $k$ -space, by generating, on a  $512^3$  grid, the density harmonics,  $\hat{\delta}(k)$ , corresponding to a  $\Lambda$ CDM power spectrum at  $z = z_i = 24$ . Once the density harmonics are generated, we take the inverse Fourier transform

Table 1. Mass and Length Filtering Scales

Filter name	$M [\text{M}_\odot]$	$R_f [\text{kpc}]$	$R_f/\Delta$	$R_f/L_{\text{box}}$
M01	$7.61 \times 10^7$	50.4	1.53	0.00299
M02	$2.53 \times 10^8$	75.2	2.28	0.00445
M03	$8.42 \times 10^8$	112.3	3.40	0.00664
M04	$2.80 \times 10^9$	167.6	5.08	0.00992
M05	$9.32 \times 10^9$	250.2	7.58	0.0148
M06	$3.10 \times 10^{10}$	373.6	11.31	0.0221
M07	$1.03 \times 10^{11}$	557.8	16.90	0.0330
M08	$3.43 \times 10^{11}$	832.7	25.23	0.0493
M09	$1.14 \times 10^{12}$	1243.1	37.66	0.0736
M10	$3.80 \times 10^{12}$	1855.9	56.22	0.110

to obtain the initial density contrast,  $\delta_i$ . This gives us our first grid in real space, with the unfiltered density contrast. To get the 10 filtered grids, we first multiply the density harmonics by the Fourier transform of the filter, and then take the inverse Fourier transform to get the filtered density contrast. Notice that in our simulations the value of the initial redshift,  $z_i$ , is actually irrelevant, as long as it is larger than the collapse redshifts of all the density peaks that are resolved in our simulations. It turns out that the first peak collapses at redshift,  $z = 18.55$ .

### 3.2. The Local Density Peaks

For each of the 10 filtered grids, we identify the location of the local density peaks. These peaks are defined as grid points where the density contrast is positive, and its value exceeds the values at the 26 neighboring grid points (taking periodic boundary conditions into account). For each density peak on each filtered grid, we compute a collapse redshift,  $z_{\text{coll}}$ , and a direction of least resistance,  $\hat{\mathbf{e}}$ . The collapse redshift is obtained by solving numerically the following equation,

$$\delta_c(z_{\text{coll}}) = \delta_i \frac{\delta_+(z_{\text{coll}})}{\delta_+(z_i)}, \quad (17)$$

where  $\delta_i$  is the initial density contrast at the peak, and  $\delta_+$  is the linear growing mode (for flat,  $\Lambda \neq 0$  models, see, e.g., Martel 1991, equation [18]). The critical value,  $\delta_c$ , is equal to 1.69 for an Einstein-de Sitter model, and slowly varies with redshift for other models. In our simulations, we simply assume  $\delta_c = 1.69$ . If equation (17) has no solution, we are simply dealing with a density peak that would collapse in the future, and we just ignore it.

To check for consistency, we performed a N-body simulation of structure formation in a box of the same size, for the same cosmological model and density fluctuation power spectrum. We used a P<sup>3</sup>M algorithm (Hockney & Eastwood 1981) with  $256^3$  equal-mass particles. The mass per particles was  $1.087 \times 10^7 M_\odot$ , hence the lowest mass scale  $M_1$  corresponds to 7 particles. We used a standard friends-of-friends algorithm (Davis et al. 1985) to identify halos at various redshifts between  $z = 24$  and  $z = 2$ . For this, we used 2 different linking lengths. We first use the “standard” value  $l = 0.25\Delta x$ , where  $\Delta x$  is the mean particle spacing. We also used a value  $l = (18\pi^2)^{-1/3}\Delta x = 0.1779\Delta x$ , corresponding to a density increase by a factor of  $18\pi^2$ . This is consistent with the assumption that collapsed, virialized halos have a density equal to  $18\pi^2$  times the mean background density (see eq. [18] below). Only halos containing 6 particles or more are included. This corresponds to a minimum mass of  $6.522 \times 10^7 M_\odot$ .

In Figure 4, we plot the numbers of collapsed halos present in the N-body simulation versus redshift (dashed lines). We find more halos with  $l = 0.25$  than with  $l = 0.1779$ . This might seem surprising since halos “break up” as  $l$  is reduced. However, many halos fall below the threshold of 6 particles when  $l$  is reduced. The two methods differ by about 20% at low redshift, but the difference increases at high redshift. The dotted line shows a calculation based on the Press-Schechter (PS) approximation (Press & Schechter 1974). The agreement with the N-body simulations is excellent at low redshift, while at very high redshifts ( $z > 15$ ) the PS approximation overestimates the number of halos. The solid line shows the number of collapsed halos in our Monte Carlo simulations. This was obtained by counting, at given redshifts  $z$ , the number of halos with  $z_{\text{coll}} > z$ , and removing the halos that have been destroyed by mergers (see §3.4 below). The number of halos is lower for the Monte Carlo simulations than for the N-body simulation or the PS approximation, at all redshifts. We interpret this result as follows: in the Monte Carlo simulations, only the matter located in overdense regions can eventually end up inside collapsed halos, while in the N-body simulations, all the

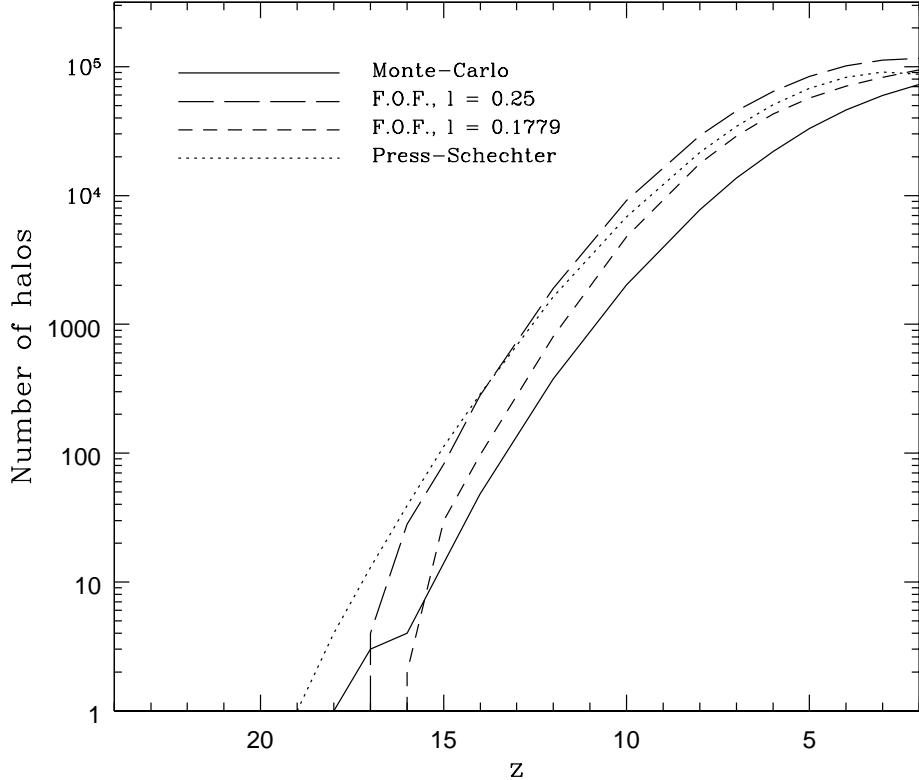


Fig. 4.— Number of collapsed halos present in the computational volume, versus redshift. *Long and short dashes:* N-body simulation with friends-of-friends algorithm, with linking lengths,  $l = 0.25\Delta x$  and  $l = 0.1779\Delta x$ , respectively; *dotted line:* Press-Schechter approximation; *solid line:* Monte Carlo simulations.

matter in the system can eventually end up in halos. Notice also that the comparison between the PS and N-body results and the Monte Carlo results is complicated by the fact that the mass spectrum of halos is discrete for the Monte Carlo simulations. For the N-body simulation and the PS approximation, the choice of an appropriate minimum mass is not obvious, and the results are quite sensitive to that choice, especially at high redshift when most halos have a small mass.

These results also vindicate our choice of an initial redshift of,  $z_i = 24$ . Clearly the system is still in the linear regime at that redshift. The very first halo collapses at redshift  $z = 18.55$  in the Monte Carlo simulations, and at redshifts,  $z = 16 - 17$ , in the N-body simulation, while the PS approximation predicts that a computational volume of that size will typically contain one halo at  $z = 19$ . Indeed, the probability of finding one halo of mass,  $M = M_1 = 7.61 \times 10^7 M_\odot$ , at  $z = 24$ , according to the PS approximation, is about 1/1000.

### 3.3. The Direction of Least Resistance

We compute, for each peak, the direction of least resistance, using the method described in §2.2. The radius,  $R^*$ , defines the region around the peak over which the least-square fit to equation (1) is performed. Its value will affect the determination of the coefficients,  $A, B, C, D, E$  and  $F$ , and ultimately the direction,  $\hat{\mathbf{e}}$ , of the outflow. The largest possible value of  $R^*$  should be the filtering scale, since this scale corresponds to the physical extent of the peak (using a larger value would amount to including matter that belongs to different peaks). As for the minimum value,  $R^*$  must clearly be at least equal to the grid spacing,  $\Delta$ . It turns out that this condition is insufficient. If  $R^* < 2^{1/2}\Delta$ , only the 6 nearest grid points to the peak are included in the fit. In that case, the matrix,  $M$ , is already diagonal, and the only directions allowed for the outflow are along the unrotated coordinate axes  $x, y, z$ . We must at least include the 12 next nearest grid points, located at a distance equal to  $2^{1/2}\Delta$  from the peak.

To test how the direction of the outflow depends on the particular choice of  $R^*$ , we considered the filters, M03, M04, ..., M10, and computed, for all peaks, two values of  $\hat{\mathbf{e}}$ : one using  $R^* = 2\Delta$ , and one using  $R^*$  equal to the filtering scale,  $R_f$ . Figure 5 shows histograms of the angle in degrees between these two values of  $\hat{\mathbf{e}}$ . For the vast majority of peaks, the angle is below 4 degrees and it exceeds 10 degrees only for very few peaks. The interpretation of these results is that our method for determining the direction of the outflow has an uncertainty of a few degrees, resulting from the ambiguity in the choice of  $R^*$ . Since we will consider outflows with opening angles of several tens of degrees, this uncertainty is inconsequential. We excluded from this test the mass filters M01 and M02, because the range of allowed values for  $R^*$  becomes very narrow.

From this test, we conclude that our technique for determining the direction of least resistance is robust, and consequently the particular value chosen for  $R^*$  is not important. Hence, we decided to set  $R^*$  equal to the filtering scale,  $R_f$ .

Once this is all done, we have, for each of the 10 filtering scales, a list of local density peaks, and for each of these peaks, a position,  $\mathbf{r}$ , a mass,  $M$  (the mass of the corresponding filtering scale), a collapse redshift,  $z_{\text{coll}}$ , and a direction of least resistance,  $\hat{\mathbf{e}}$ . In the model, each peak corresponds to a density fluctuation of mass,  $M$  (the filtering mass), and radius,  $R_f$  (the filtering radius). If left alone, this peak will collapse at redshift,  $z_{\text{coll}}$ , to form a halo of mass,  $M$ , located at position,  $\mathbf{r}$ . This protogalaxy will eventually turn into a galaxy (by forming stars), and generate an outflow propagating along the direction of least resistance,  $\hat{\mathbf{e}}$ .

### 3.4. Formation of First-Generation Galaxies

The 10 filtered grids represent the same region of the universe. Hence, we cannot simply assume that every peak collapses to form a protogalaxy, since this would violate conservation of mass. We must deal with the issue of halos inside halos.<sup>1</sup> Consider two density peaks  $a$  and  $b$  of masses,  $M_a < M_b$  (these peaks are therefore on different grids). If the separation,  $|\mathbf{r}_a - \mathbf{r}_b|$ , between the peaks is smaller than the filtering scale,  $R_{f,b}$ , of the larger mass, the two halos that these peaks will form cannot coexist, since the smaller halo is inside the larger one. There are then two possibilities, depending on the collapse redshifts. If  $(z_{\text{coll}})_b > (z_{\text{coll}})_a$ , then halo  $a$  will never form, since all the matter it contains will be incorporated into halo  $b$ , that forms earlier. While this does occur it is not common, since in a CDM universe smaller peaks tend

---

<sup>1</sup>Throughout this paper, we shall use the term “halo” to designate a collapsed object, whether it is a galaxy or a protogalaxy.

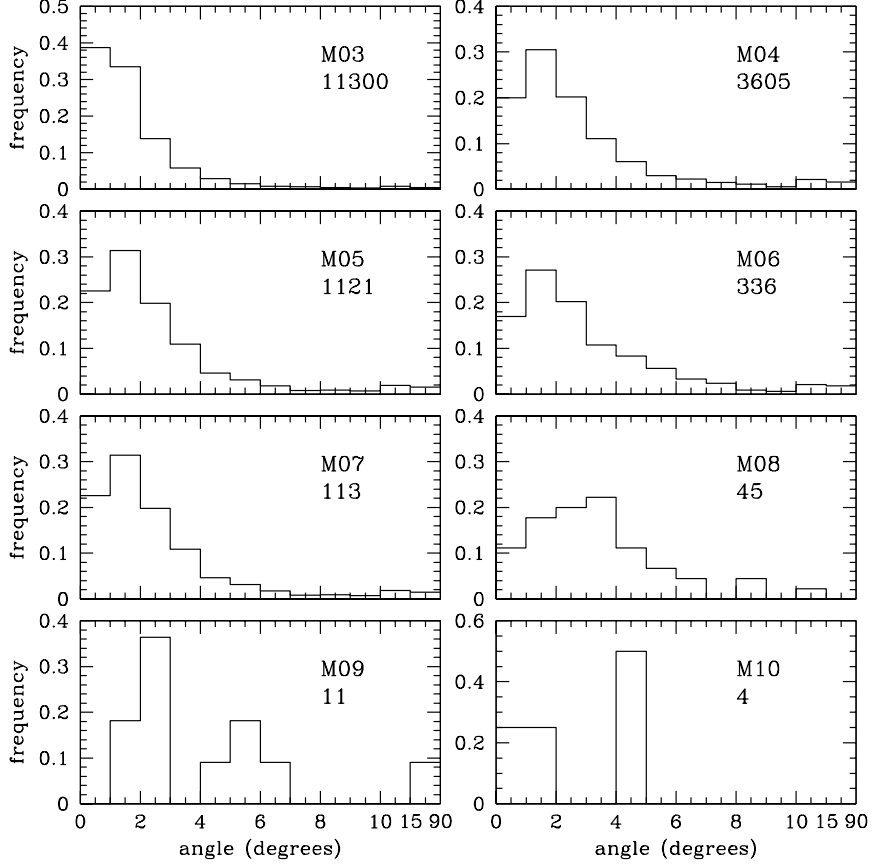


Fig. 5.— Histograms of the fluctuations in the direction of the outflows resulting from variations in  $R^*$ . Notice that the last two bins correspond to the ranges [10,15] degrees and [15,90] degrees, respectively. The labels in the panels indicate the mass filtering scale and the number of peaks.

to collapse earlier than bigger ones. The second possibility is  $(z_{\text{coll}})_a > (z_{\text{coll}})_b$ . In this case, halo  $a$  will form first, at redshift  $(z_{\text{coll}})_a$ , but will be destroyed later by a *merger event* at redshift,  $(z_{\text{coll}})_b$ , that results in the formation of halo  $b$ . So, even though halos remain at fixed locations in this simplified Monte Carlo model, non-dynamic merger events are included.

The collapse of a peak leads to the formation of a halo, which we identify as a protogalaxy. The gas inside that halo is at the virial temperature, given by

$$T_{\text{vir}} = \frac{0.009 \text{ K}}{\beta} \left( \frac{6.8}{5X + 3} \right) \left( \frac{Mh}{1 \text{ M}_\odot} \right)^{2/3} (1 + z_{\text{coll}}) \left[ \frac{\Omega_0}{\Omega(z_{\text{coll}})} \right]^{1/3} \left[ \frac{\Delta_c(z_{\text{coll}})}{18\pi^2} \right]^{1/3}, \quad (18)$$

(Eke, Cole, & Frenk 1996), where  $X = 0.76$  is the hydrogen mass fraction, and  $\Delta_c$  is the ratio of the halo's mean density to the critical density. Since this temperature is usually much too large to allow the formation of stars, the gas must cool down to a temperature,  $T \ll T_{\text{vir}}$ , before stars form and the protogalaxy becomes a galaxy. As in SB01, we use the cooling model of White & Frenk (1991). This model assumes that the

cooling proceeds inside-out. The gas inside a “cooling radius”,  $r_{\text{cool}}$ , has cooled, while the gas outside  $r_{\text{cool}}$  remains hot. As  $r_{\text{cool}}$  increases with time, the mass,  $M_{\text{cool}}$ , of cool gas increases, until all the gas has cooled. The mass,  $M_{\text{cool}}$ , evolves according to

$$\frac{dM_{\text{cool}}}{dt} = 12 \left( \frac{\Omega_{b,0}}{\Omega_0} \right)^{3/2} f_0 \left( \frac{T_{\text{vir}}}{1 \text{ K}} \right) [\Lambda_{23}(T_{\text{vir}}, Z)]^{1/2} \left( \frac{t}{1 \text{ yr}} \right)^{-1/2} M_{\odot} \text{ yr}^{-1}, \quad (19)$$

where  $\Lambda_{23}$  is the cooling rate in units of  $10^{-23} \text{ ergs s}^{-1} \text{ cm}^{-3}$ , which is a function of temperature and metallicity,  $Z$ , and  $f_0 \approx 0.8$  (a correction factor suggested by Somerville 1997 to bring this result into line with more complex analyses). We determine the required cooling rate using MAPPINGS III<sup>2</sup>, a successor to MAPPINGS II outlined in Sutherland & Dopita (1993). We integrate both sides between  $t = 0$  and  $t = t_{\text{cool}}$ , the cooling time. For a halo of mass,  $M$ , and gas mass,  $M_{\text{gas}} = \Omega_{b,0} M / \Omega_0$ , we get

$$t_{\text{cool}} = \frac{1}{576 f_0^2} \left( \frac{M}{1 M_{\odot}} \right)^2 \left( \frac{\Omega_{b,0}}{\Omega_0} \right)^{-1} \left( \frac{T_{\text{vir}}}{1 \text{ K}} \right)^{-2} [\Lambda_{23}(T_{\text{vir}}, Z)]^{-1} \text{ yr}. \quad (20)$$

Note that for halos with circular velocities  $< 75 \text{ km s}^{-1}$  ( $T_{\text{vir}} < 2 \times 10^5 \text{ K}$ ) photoionization by the UV background heats the gas and prevents it from cooling with atomic hydrogen lines (e.g. Thoul & Weinberg 1996). We take a conservative estimate of this effect and assume that these halos form in regions that are reionized at  $z = 6$ .

Using the solution of the Friedman equation for our  $\Lambda \text{CDM}$  model, we compute, for each halo, the epoch,  $t_{\text{coll}}$ , at which collapse occurs from the collapse redshift,  $z_{\text{coll}}$ . We then add the cooling time to get the epoch at which galaxy formation occurs,  $t_{\text{gf}} = t_{\text{coll}} + t_{\text{cool}}$ , and compute the corresponding galaxy formation redshift,  $z_{\text{gf}}$ . The galaxy formation epoch may be later than the current epoch, in which stars will not form and the halo will remain a protogalaxy, unless metal deposition from outflows modifies the cooling rate (see below).

We refer to these galaxies as “first-generation” galaxies since at the time of formation they are untouched by impinging outflows from other galaxies. For these galaxies we assume a cooling rate based on zero metallicity. In the following section we will discuss galaxies for which this is not the case.

We are now ready to proceed with the simulation. Starting at initial redshift  $z_i = 20$ , we evolve the system forward by redshift steps of  $\Delta z = -0.005$ . As a result we take 3600 steps to reach the end point for our simulations which is  $z = 2$ . This end point is chosen for comparison with Quasar absorption spectra data from  $z = 2 - 6$ . Also, our box would no longer represents a cosmological volume at lower redshifts.

At the location of each peak  $a$ , a halo forms at redshift,  $(z_{\text{coll}})_a$ , unless that peak was located inside a larger peak that collapsed first, as described above. During the redshift interval,  $[(z_{\text{coll}})_a, (z_{\text{gf}})_a]$ , while the gas is cooling, the halo might be destroyed by a merger. This will happen if there is a peak  $b$  for which

$$M_b > M_a, \quad (21)$$

$$(z_{\text{coll}})_a > (z_{\text{coll}})_b > (z_{\text{gf}})_a, \quad (22)$$

$$|\mathbf{r}_a - \mathbf{r}_b| < R_{f,b}. \quad (23)$$

In this case, the halo was able to form, but did not manage to cool before being destroyed, hence the actual galaxy never formed.

---

<sup>2</sup><http://www.mso.anu.edu.au/~ralph/map.html>

If the galaxy does manage to form, we neglect the formation time and life span of massive stars and so the newly formed galaxy immediately produces an outflow centered at the halo position,  $\mathbf{r}_a$ , and propagating along the direction,  $\hat{\mathbf{e}}_a$ . We evolve this outflow with time, using the solutions given in Appendix A (with timesteps corresponding to our redshift steps,  $\Delta z = -0.005$ ).

Left alone, the outflow will go through the successive phases of driven expansion by supernovae, snowplow, and Hubble expansion. However, during any of these stages, the galaxy producing the outflow might be destroyed by a merger. In all such cases the outflow reverts to a Hubble expansion phase.

### 3.5. Subsequent Galaxy Formation

After the first outflows are formed, some will begin to strike other density peaks<sup>3</sup> and modify the way these systems evolve. They may enrich these systems with new metals, possibly modifying their cooling time. They may also expel the gas content of the object by ram pressure stripping or shock-heating of the gas. Of these two mechanism, the former (stripping) is the dominant one (Scannapieco, Ferrara, & Broadhurst 2000) and so we will neglect the latter.

#### 3.5.1. Stripping

Density peaks may be stripped of their baryons when the swept-up shell of intergalactic gas incident upon them imparts sufficient momentum on the baryons such that they escape the potential well of the peak, i.e.

$$\left( \frac{l^2}{4R^2} \right) M_o v_o \geq M_b v_{\text{esc}}, \quad (24)$$

where the mass of the swept up shell is  $M_o$  at radius,  $R$ , (as in TSE),  $v_o$  is the outflow velocity,  $M_b$  is the baryonic mass of the density peak struck, and  $v_{\text{esc}}$  is the escape velocity for successfully stripped gas.  $l$  is the comoving radius of the collapsing density peak. Using the spherical approximation for gravitational collapse this scale is determined from the non-linear density contrast,  $\delta_{\text{NL}}$  using  $l = R_f(1 + \delta_{\text{NL}})^{-1/3}$  where  $1 + \delta_{\text{NL}} = 9(\theta - \sin \theta)^2/[2(1 - \cos \theta)^3]$ . The parameter,  $\theta$ , is in turn given by

$$\left( \frac{\theta - \sin \theta}{2\pi} \right)^{2/3} = \frac{\delta_+(z)}{\delta_+(z_{\text{coll}})}, \quad (25)$$

where  $\delta_+(z_{\text{coll}})$  and  $\delta_+(z)$  are the linear growing modes at collapse and when the outflow strikes the peak respectively.

We assume that stripping may only occur for systems that have not collapsed since the cross section to impact is small resulting in negligible momentum transfer. This approach is supported by Sigward, Ferrara, & Scannapieco (2005) who investigate this issue with a numerical analysis of an individual object struck by a shock. It is also worth noting that we deal with baryonic stripping in the same way whether or not the source galaxy is within the filtering radius of the density peak struck (although it is less likely to occur due the larger escape velocity and mass of the halo struck).

---

<sup>3</sup>In the following text we will use the term “peaks” to refer to density peaks that will go on to form halos by  $z = 0$ .

When the criterion for stripping is met, the density peak is rendered free of baryons and, while it may collapse, it will not form a galaxy. If the shell of the outflow does not strip the peak it is enriched by the metal-rich gas of the outflow cavity ejected by the galaxy.

### 3.5.2. Metal Enrichment

Metals are propagated throughout our simulations within the hot bubbles of outflows. Peaks which have not been struck by outflows are assumed to have metallicity of  $[\text{Fe}/\text{H}] = -3$  which is negligible for the purposes of calculating the halo cool time. Once galaxies are formed metals are produced at rate of  $2\text{M}_\odot$  per SN (Nagataki & Sato 1998). Hence the mass of metals in the outflow is

$$M_Z = f_{\text{esc}} \frac{2\text{M}_\odot}{M_{\text{req}}} f_* \frac{\Omega_{b,0}}{\Omega_0} M, \quad (26)$$

where  $f_{\text{esc}}$  is the mass escape fraction of the outflow. We use the value  $f_{\text{esc}} = 0.5$  taken from the numerical simulations of Mori, Ferrara, & Madau (2002). This mass of metals is distributed evenly throughout the volume of the outflow.

It is notable that in this calculation the ratio of the rate of gas mass lost due to winds to the rate at which gas mass is turned into stars is  $f_{\text{esc}} M_{\text{SN}}/M_{\text{req}} \sim 0.05$ . This does not include the mass lost due to gas swept up by the outflows, but this will be negligible in our model as we assume that all material swept up is at the mean density of the IGM. We currently make no correction for sweeping up of the ISM. Observations indicate that this ratio is expected to be of order 1 for local starburst galaxies (e.g. Heckman et al. 2000) but it is unclear whether this is a requirement at redshifts,  $z > 2$  where most of the significant galactic outflows occur.

When an outflow strikes an uncollapsed density peak and does not strip it, it modifies its metal content. It deposits a fraction of its metals,  $f_{\text{dep}} V_{\text{overlap}}/V_{\text{outflow}}$ , where  $f_{\text{dep}}$  is a mass deposition efficiency which we set at  $f_{\text{dep}} = 0.9$ ,  $V_{\text{overlap}}$  is the volume of overlap of the uncollapsed density peak of radius  $l$ , and  $V_{\text{outflow}}$  is the volume of the outflow. This volume of overlap is calculated based on various geometric approximations to the overlap of two spherical cones and a sphere, depending on their relative size and orientation. Once the halo has collapsed, the addition of metals results in an increase in cooling rate and so a reduction in the cooling time, expediting galaxy formation.

We assume that the SNe in our simulations are only of the Type II variety since these SNe explode together shortly after the starburst and lead to a coherent extragalactic outflow which will reach large distances. As a result we use an alpha element rich yield of metals [quoted in Sutherland & Dopita (1993) as “primordial” abundance ratios] and distribute our mass of metals accordingly. This provides a value for  $[\text{Fe}/\text{H}]$  used to calculate the new cooling rate.

In the special case where an outflow strikes a density peak while the source galaxy itself is within it, the volume overlap is assumed to be 100%. However, if this outflow goes on to escape this combined system, metals will still be deposited in the IGM and other density peaks due to the non-unity mass deposition efficiency. The main motivating factor behind the inclusion of the mass deposition efficiency is to avoid the implausible scenario that an outflow may continue to grow having left all its metals behind. The value it should take is unknown, however, the simulations are not sensitive to this factor, as we point out below.

## 4. RESULTS

### 4.1. The Impact of Varying Opening Angle

We have constructed a model for the evolution of anisotropic outflows and a testbed with which to investigate its significance and we are now ready to discuss what this approach tells us.

Taking an extreme case of anisotropy as an illustration, consider an opening angle of only  $40^\circ$  at the natural end point of our simulations,  $z = 2$ . We show in Figure 6 a slice of thickness  $0.4h^{-1}\text{Mpc}$  through our simulation box. The position and extent of our galactic outflows are indicated along with the position and pre-collapse radius of peaks (i.e. the filtering scale,  $R_f$ , of the peak) that will collapse by  $z = 0$ . These outflows extend a significant distance from their source galaxies and often strike other peaks. Where peaks are arranged in a row in the plane of the slice, the outflows appear to favor a direction perpendicular to this structure (see zoom in). This is to be expected: the locations of these galaxies trace the underlying structure of a dense filament out of which they would have formed by fragmentation (in a more realistic simulation), and the outflows follow the path of least resistance away from that filament.

Figure 7 shows the counts of various quantities in units of  $(h^{-1}\text{Mpc})^{-3}$  by  $z = 2$ , for varying opening angle. The number density of peaks that are hit by outflows which will go on to form halos by  $z = 0$  are shown. This decreases as approximately a power law for increasingly anisotropic outflows which can be explained by two factors; anisotropic outflows take a path of least resistance out of highly overdense regions and so will encounter less regions that go on to form halos. Also the total volume occupied by outflows is not conserved for varying opening angle since anisotropic outflows tend to overlap less (see above) and the volume per outflow is not constant. The degeneracy between these two effects is resolved in Figure 8 and the accompanying text. The number density of peaks stripped of their baryons is also shown and indicates that the fraction of peaks hits which are then stripped is roughly constant ( $\sim 80\%$ ).

The number of galaxies formed by  $z = 2$  rises smoothly for decreasing opening angle in Figure 7 as a result of the fall in stripping. We find that metal enrichment of peaks has a negligible impact on the number of galaxies, however those galaxies which form are born slightly earlier. Not all peaks which are hit by outflows but not stripped will go on to produce galaxies by  $z = 2$ . This is because, despite being enriched by metals and collapsing, their baryons do not cool to form stars by this redshift. As a result, the incidence of stripping decreases faster than the number of galaxies increases. This is demonstrated with the sum of these two number densities in Figure 7 which decreases with increasingly anisotropic outflows.

In Figure 8 we show various statistics at  $z = 2$  in the simulations; (from top left to bottom right) the average distance,  $\bar{R}_{\text{strip}}$ , traveled by outflows before stripping occurs, the maximum distance,  $R_{\text{max}}$ , traveled by an outflow, the estimated volume filling factor of outflows, and the ratio of the number density of hits to the volume filling factor in units  $(h^{-1}\text{Mpc})^{-3}$ . The mean distance traveled by outflows before stripping occurs is flat until  $100^\circ$  where it begins to rise. As the anisotropic outflows travel farther with decreasing opening angle, they fail to hit new peaks as they have already escaped their highly overdense environments. It is only when  $\alpha = 100^\circ$  that they begin to reach the next dense structure.

In the top right panel we show the radius of the largest outflow for each opening angle. We also show a curve for constant volume using equation (9), which gives  $R \propto 1/[1 - \cos(\alpha/2)]^{1/3}$ . This shows that while the radius of outflows goes up with decreasing opening angle it does not go up fast enough to conserve the volume per outflow.

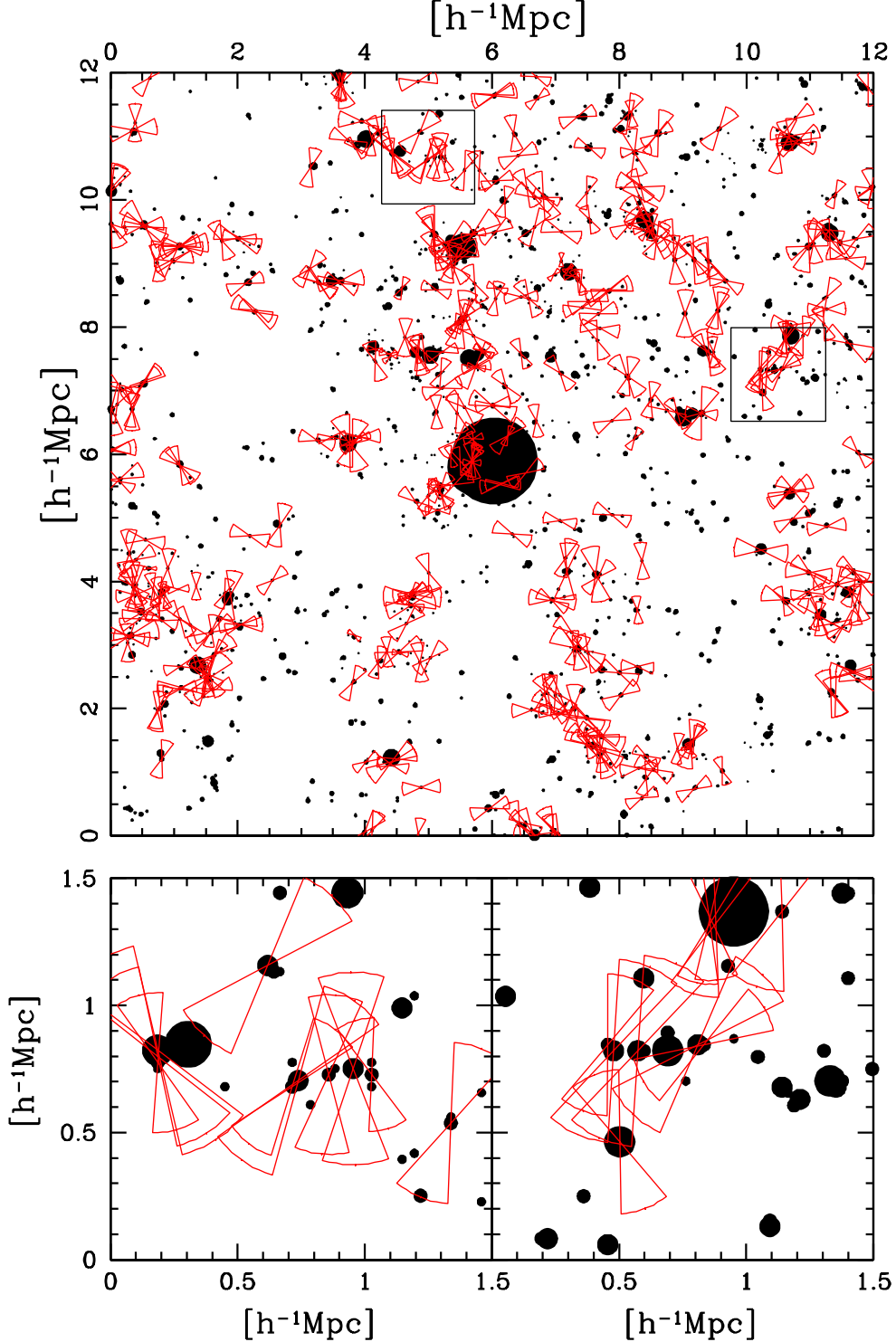


Fig. 6.— A slice through the simulation box of thickness  $0.4h^{-1}\text{Mpc}$  at  $z = 2$ . Density peaks are shown as filled circles of diameter corresponding to their extent prior to collapse. The location and physical coverage of outflows are indicated as red wedges which have an opening angle of  $40^\circ$ . Two zoom-in regions of size  $1.5h^{-1}\text{Mpc}$  show regions of interest, where galaxies that formed out of a common filament produce outflows that are aligned.

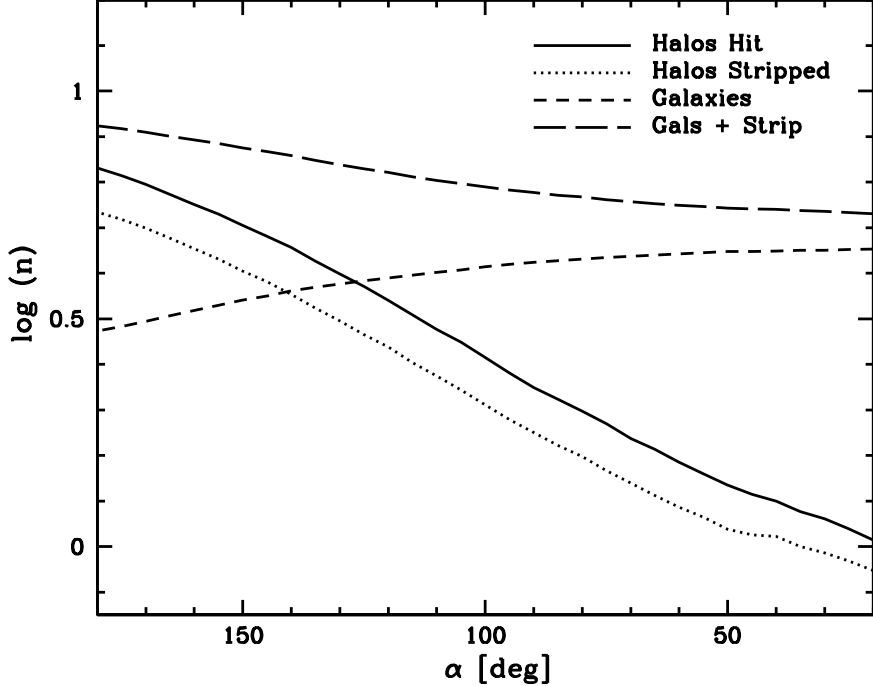


Fig. 7.— The number density of various objects in units  $(h^{-1}\text{Mpc})^{-3}$  at  $z = 2$ , versus opening angle. *Solid line* : number of peaks hit that will go on to collapse before  $z = 0$ ; *dotted line* : number of those peaks which are then stripped of their baryons; *short dashed line* : number of galaxies; *long dashed line* : sum of the number of galaxies and stripped peaks.

The estimate of the volume filling factor is calculated based on the sum of the volume of all outflows, with a correction factor for the increasing probability of overlap, as these outflows grow using the relation

$$F = 1 - \exp \left[ -\frac{\sum_{i=1}^{N_o} V_i}{(12h^{-1}\text{Mpc})^3} \right], \quad (27)$$

where  $V_i$  is the volume per outflow given by equation (9) and  $N_o$  is the number of outflows. The volume filling factor rises to a peak at  $\alpha = 100 - 120^\circ$ . As indicated above, the volume per outflow is not conserved with varying opening angle and the volume of the enriched region actually decreases for increasingly anisotropic outflows. As a result one would naively expect the volume filling factor to fall for decreasing  $\alpha$ , however, since the number of galaxies increases faster than the volume per outflow goes down in this regime, the volume filling factor increases.

Figure 7 indicates that the number density of peaks hit decreases from  $180^\circ - 20^\circ$ , but so does the volume filling factor (Fig. 8). We can use both these statistics to determine the impact of opening angle on the change in the number of peaks hit resulting from the path of least resistance of the outflows. We do this by taking the ratio of the number density of hits to the volume filling factor, shown in Figure 8; this is the number of hits per volume covered by outflows. This indicates that as outflows become more anisotropic they tend to avoid high-density structures and favor voids until  $\alpha \approx 50$  when this statistic turns around, indicating that most outflows have crossed voids and have reached the next overdense structure. These statistics indicate that galactic outflows undergo a transition over the range  $\alpha = 100^\circ - 50^\circ$ , from

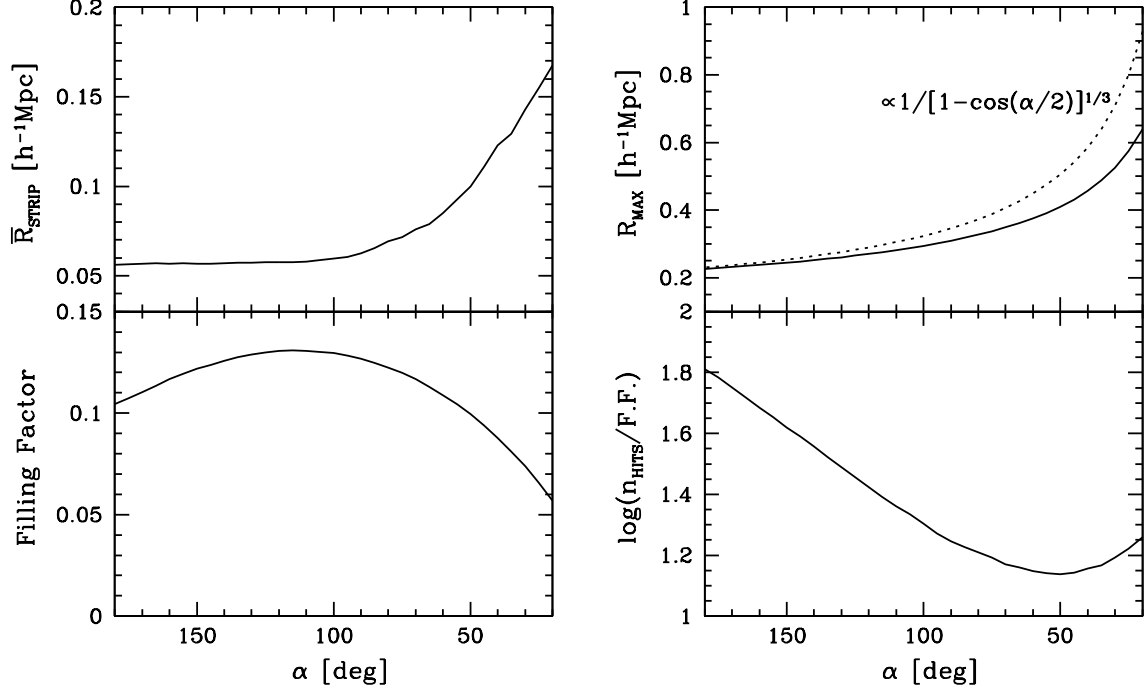


Fig. 8.— *Top left* : mean radius of outflows when they strip peaks of their baryons; *top right*: the *solid line* shows the radius of the largest outflow and, for comparison, the *dotted line* shows  $R \propto 1/[1-\cos \alpha/2]^{1/3}$  which is the relation expected if the volume enriched were conserved for varying opening angle. The estimated volume filling factor is shown in the *bottom left* panel; *bottom right* : the ratio of the number density of peaks hit to the volume filling factor in units of  $(h^{-1}\text{Mpc})^{-3}$ .

enriching their own high-density sources and the surrounding voids, to enriching neighboring high-density regions after crossing the voids. The top right panel indicates that in this range the radius of the largest outflow increases from around  $0.3 - 0.4 h^{-1}\text{Mpc}$  compared to the isotropic case of  $0.23 h^{-1}\text{Mpc}$ , confirming the plausibility of this explanation.

#### 4.2. Enrichment of Overdense and Underdense Systems

We have established that the volume filling factor of enriched regions is sensitive to the anisotropy of galactic outflows but what is the nature of regions enriched? We investigate this by returning to the original, unsmoothed, density field produced with a Gaussian random realization of structure. This density field is a result of purely linear evolution from initial conditions with a Gaussian probability distribution function (PDF). We map to a lognormal PDF in order to mimic a degree of non-linear behavior which has been found to reproduce the PDF of the density in SPH simulations well (Bi & Davidsen 1997). The success of this approach is limited by the incomplete description of clustering.

Having scanned through all  $512^3$  grid points in the mapped density field, we determined whether any of the galactic outflows reach them. Where this is the case we have flagged them as enriched and note their overdensity. In Figure 9 we show three statistics derived from this approach for a range of different

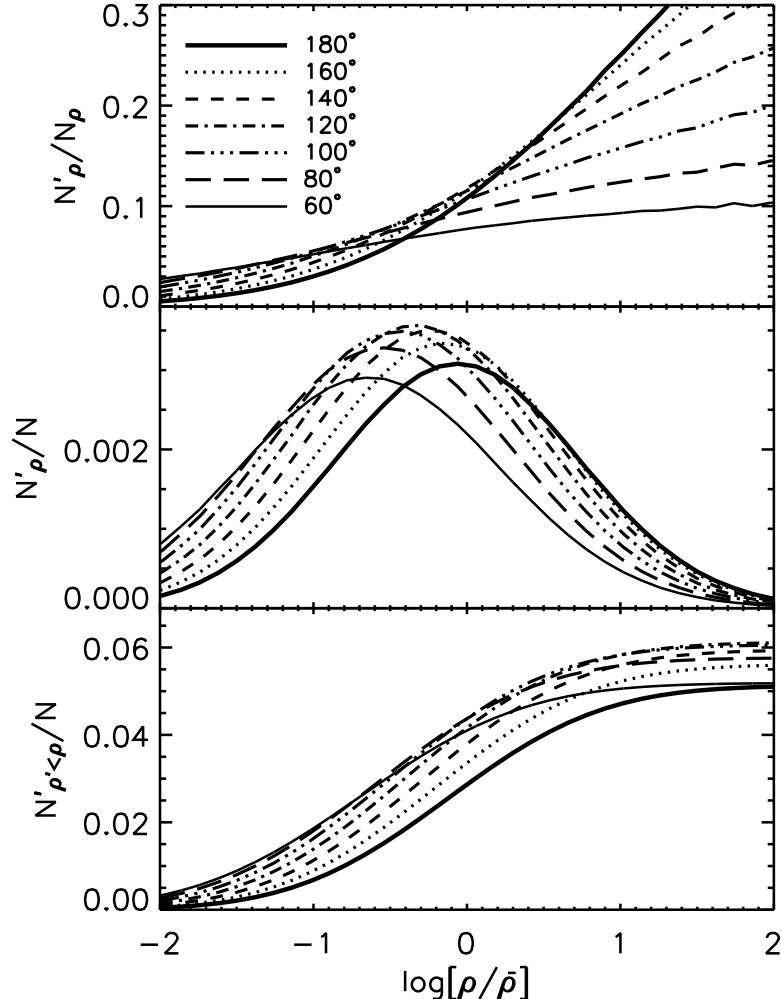


Fig. 9.— The number of enriched grid points  $N'_\rho$  in the simulation volume at  $z = 2$  as a function of IGM overdensity for varying opening angle. In the *top* panel this is shown as a fraction of the number of systems at this density,  $N_\rho$ . The statistic as a function of the total number of points,  $N$ , is shown in the *middle* panel. The *bottom* panel shows the number of enriched points below an overdensity threshold,  $N'_{\rho'<\rho}$ .

opening angles from  $60^\circ - 180^\circ$ . We show (from top to bottom) the number of grid points enriched at a given overdensity,  $N'_\rho$ , as a fraction of the number of grid points at that density,  $N_\rho$ ; this is effectively the probability of enriching a system of a given density. This panel indicates that the effect of galactic outflows on overdense systems is dramatically reduced for increasingly anisotropic outflows. This is quite plausible in the context of the low number density of overdense systems. It is also clear that for decreasing opening angle the probability of enriching low density systems increases.

The middle panel shows the number of grid points enriched at a given overdensity as a fraction of the total number of grid points,  $N$ . In a plot of  $\log(\rho/\bar{\rho})$  these curves are Gaussian reflecting the underlying density PDF. The mean of the Gaussian drifts to lower densities for lower opening angles. The amplitude of this Gaussian is maximum for  $\alpha = 120^\circ$ . The bottom panel is a cumulative version of the middle panel and so indicates the number of enriched grid points with an overdensity below a given threshold,  $N'_{\rho'<\rho}$ . This highlights the significant impact on the enrichment of underdense systems of anisotropic outflows.

Anisotropic outflows can lead to an increase of 50% in the extent of enrichment of underdense systems in the case where  $\alpha = 100^\circ - 120^\circ$ . Also, the real volume filling factor of outflows (rather than the estimate shown in Figure 8) can be read off the point where the curves meet the right hand axis since there are very few grid points with  $\rho/\bar{\rho} > 100$ . The volume filling factor peaks when  $\alpha = 120^\circ$  at just over 6% and explains the peak in amplitude seen in the middle panel.

## 5. DISCUSSION

There is a degree of uncertainty for the parameters  $f_*$ ,  $f_w$ ,  $f_{\text{dep}}$ ,  $f_{\text{esc}}$  and they are of varying importance. The star formation efficiency,  $f_*$ , has a well-documented and large uncertainty. It has a significant affect on the predicted volume filling factor as outlined in SFM. Our quoted values for the volume filling factor should be considered with this in mind. However, the dependance on opening angle is a stronger claim and while the point of the turnover may vary, the shape will remain unchanged. The fraction of total supernova energy goes into the outflow,  $f_w$ , and the mass escape fraction,  $f_{\text{esc}}$ , both have associated uncertainties but have been constrained by SFW (and references therein) and Mori, Ferrara, & Madau (2002). The value for the efficiency with which outflow metals are deposited upon collapsing density peaks,  $f_{\text{dep}}$ , is poorly constrained and requires further analysis. This is not a concern here as the metal enrichment does not have a significant impact on the cooling times of subsequent protogalaxies.

In the calculation of external pressure we assume that helium is singly-ionized, but Choudhury & Ferrara (2005) find that for  $z > 7$  and for  $z < 4$  helium is doubly-ionized. This was determined before the release of the 3-Year WMAP results and may be subject to change. We also assume that the IGM is at the mean density and temperature. These factors will test the accuracy of the external pressure calculation and we will seek to investigate them in further work.

The results from the previous section consistently indicate that we successfully describe anisotropic outflows which take a path of least resistance out of regions with a high number density of peaks and high overdensity such as pancakes and filaments and into voids. If sufficiently anisotropic ( $\alpha \lesssim 100^\circ$ ) these outflows will also begin to strike neighboring overdense structures and further peaks. The number of peaks hit drops for anisotropic outflows and diminishes the ability of these outflows to strip peaks of their baryons. This reduces the capacity for baryonic stripping as an explanation for the abundance of dwarf galaxies in the Local Group.

We find a quite low value for the volume filling factor of 5% – 6% but this is sensitive to a number of factors such as the star formation efficiency and the degree of clustering of source galaxies and we will present a more thorough analysis of the absolute value of this quantity in future papers in this series. We do, however, expect its dependence on opening angle of outflows to be rigorous. We find that anisotropic galactic outflows can potentially fill  $\sim 25\%$  greater a volume of the universe than their isotropic counterparts reaching this volume for opening angles of  $110^\circ - 120^\circ$ . This is an unexpected result and indicates that anisotropic outflows are a more effective way of maximizing the volume filling factor and enriching larger volumes of the Universe.

Despite this small volume filling factor, we find significant enrichment of underdense systems (whose density is at or below the mean density of the Universe), particularly when these outflows are anisotropic. The volume filling factor of enriched underdense systems is maximized by a opening angle of  $100^\circ - 120^\circ$ , this is  $\sim 50\%$  higher than that for isotropic outflows. This may provide an explanation for observations of metal enrichment in systems at or around the mean density as seen in Schaye et al. (2003) and Pieri &

Haehnelt (2004) without the need to appeal to large volume filling factors. These outflows also reach larger distances from their source galaxies and may aid in the explanation of why metal enrichment is seen far from observed galaxies (Pieri, Schaye, & Aguirre 2006). Since parts of the IGM are enriched solely based on whether they are located in the path of least resistance of an outflow, this may provide a further source of scatter in the metallicity of the IGM as yet unexplained in simulations as pointed out Pieri, Schaye, & Aguirre (2006). In a subsequent paper of this series (Pieri, Grenon, & Martel 2006) we will investigate these issues by performing a direct comparison between these observations and synthetic QSO absorption spectra produced using our analytic description of anisotropic outflows.

The strongest and weakest points of our method are the high dynamical range and the lack of gravitational dynamics, respectively. On the one hand, the ratio of the largest to smallest mass scale we consider is  $M_{10}/M_1 \approx 50,000$ . It would be very challenging for a numerical simulation to achieve such large dynamical range in mass (that is, simulating  $L_*$  galaxies *and* dwarf galaxies together), while having sufficient resolution to properly simulate the outflows originating from the smallest galaxies. On the other hand, the treatment of large-scale structure and galaxy formation in the Monte Carlo method is quite simplistic. We combine a Gaussian random density field with a spherical collapse model for galaxy formation. In this approach, galaxies form at the comoving locations of density peaks, and remain at these locations afterward. Even though we have a prescription for destruction of galaxies by mergers, the actual clustering of galaxies is not taken into account. If galaxies were allowed to cluster, collision and stripping by outflows would be more frequent, and also it would become more difficult to enrich low-density regions with metals. This lack of a correct description of dynamics means that the description of clustering of the IGM is also limited.

The main limitation of this work is not the outflow model, but rather the Monte Carlo model used for describing galaxy formation. In two forthcoming papers (Martel, Grenon, & Pieri 2006; Pieri, Grenon, & Martel 2006), we will replace this Monte Carlo model by a more realistic numerical simulation of galaxy formation in a cosmological volume.

## 6. SUMMARY AND CONCLUSION

We have designed an analytical model for anisotropic galactic outflows based on the hypothesis that such outflows are bipolar and follow the path of least resistance in the environment their source. This analytical model has only one free parameter: the opening angle  $\alpha$ . We combined this model with a semi-analytical Monte Carlo method for simulating galaxy formation, galaxy mergers, and supernova feedback. With this combined algorithm, we study the evolution of the galaxies and the IGM inside a comoving cosmological volume of size  $(12h^{-1}\text{Mpc})^3$ , from redshifts,  $z = 24 - 2$ , in a  $\Lambda\text{CDM}$  model. Our main results are the following:

- Galaxy formation starts at redshift,  $z \sim 18$ . Since we neglect the formation and evolutionary times of massive stars, each newly formed galaxy immediately produces an outflow, which last for a time,  $t_{\text{burst}} \sim 50\text{Myr}$ . Such outflows can travel hundreds of kiloparsecs, and eventually collide with other objects. We neglect the effect of a collision with a well-formed galaxy (the cross-section is too small). When an outflow collides with a peak still in the process of collapsing, removal of the gas by ram pressure, preventing the formation of the galaxy, occurs about 80% of the time. When stripping does not occur, the protogalaxy is enriched in metals. This processus occurs for all opening angles  $\alpha$ , and the proportions 80% stripped, 20% metal-enriched is essentially independent of  $\alpha$ .

- When metal-enrichment of a peak occurs and this peak collapses to form a halo, the cooling time of that halo is reduced, and the galaxy forms earlier. However, this effect is rather small. In particular, we did not find that metal-enrichment could “bring to life” low-mass protogalaxies whose cooling time exceeds the age of the universe.
- Anisotropic outflows channel matter preferentially into low-density regions, away from the cosmological structures (filaments or pancakes) in which the galaxies producing the outflows reside. Consequently, the number of halos hit by outflows decreases with decreasing opening angle. This reduction in number of hits results in a larger number of galaxies forming, since fewer halos are stripped by the ram pressure of outflows.
- The filling factors of outflows (that is, the volume fraction of the IGM occupied by outflows) increases, then decreases with opening angle, indicating the presence of competing effects. For opening angles  $\alpha = 180^\circ - 110^\circ$ , the increase in the number of galaxies forming results in an increase in the filling factor. At smaller angles, the volume of individual outflows drops significantly with  $\alpha$ , and the total filling factor decreases since the volume per outflow decreases faster than the number of galaxies increases.
- The decrease in filling factor with decreasing angle is not sufficient to explain the decrease in number of hits. The ratio (number of hits)/(filling factor) decreases with decreasing angles down to  $\alpha \sim 50^\circ$ . This indicates that at these angles, the outflows are efficient at avoiding collisions with halos and channel matter preferentially into low-density region. Hence, if several halos reside in a common cosmological structure, an outflow produced by one of them will tend to avoid hitting the others. For angles  $\alpha < 50^\circ$ , we observe the opposite trend: outflows become more efficient in finding halos and hitting them. These narrow outflows can travel across cosmological voids and hit halos located in unrelated structures, like the next filament or pancake. This effect is a continuation of a process begun at  $\alpha \sim 100$  where the mean distance travelled by outflows when they strip collapsing peaks of their baryons begin to increase as the first neighboring structures are hit.
- The enrichment of the IGM with metals favors high-density systems since the sources of outflows are located in high-density regions. However, as the opening angle decreases, there is a dramatic reduction of the enrichment of such systems, combined with a dramatic increase in enrichment of low-density systems. Anisotropic outflows may enrich up 50% larger a volume of the underdense Universe than isotropic outflows.

All these results are a mere consequence of the fact that outflows follow the path of least resistance. This is an assumption in our model, which is motivated by observations as well as high-resolution simulations.

This work benefited from stimulating discussions with A. Ferrara, E. Scannapieco, J. Silk, M. Tegmark, R. Thacker, and S. D. M. White. All calculations were performed at the *Laboratoire d’astrophysique numérique*, Université Laval. Figure 2 was produced at the *Center for Computer Visualization*, University of Texas, by Marcelo Alvarez. We thank the Canada Research Chair program and NSERC for support. CG is also supported by a Hubert Reeves fellowship.

## A. NUMERICAL SOLUTION FOR THE OUTFLOW

The equations governing the evolution of the outflow are

$$\ddot{R} = \frac{8\pi(p - p_{\text{ext}})G}{\Omega_b H^2 R} - \frac{3}{R}(\dot{R} - HR)^2 - \frac{\Omega H^2 R}{2} - \frac{GM}{R^2}, \quad (\text{A1})$$

$$\dot{p} = \frac{L(t)}{2\pi R^3[1 - \cos(\alpha/2)]} - \frac{5\dot{R}p}{R}. \quad (\text{A2})$$

We define  $t = 0$  as the time when the outflow starts. In the limit  $t \rightarrow 0$ , we have  $R \rightarrow 0$ ,  $H \rightarrow H_i$ ,  $\Omega_b \rightarrow \Omega_{b,i}$ ,  $\Omega \rightarrow \Omega_i$ , and  $L \rightarrow L_i$ . The gravity term, Hubble terms, and external pressure term are negligible (in the sense that they diverge slower than the other terms), and equation (A1) reduces to

$$\ddot{R} = \frac{8\pi p G}{\Omega_{b,i} H_i^2 R} - \frac{3\dot{R}^2}{R}, \quad t \rightarrow 0. \quad (\text{A3})$$

We can easily show that the solutions of equations (A2) and (A3) are power laws,

$$R = Ct^{3/5}, \quad (\text{A4})$$

$$p = \frac{21\Omega_{b,i} H_i^2 C^2}{200\pi G} t^{-4/5}, \quad (\text{A5})$$

where

$$C = \left\{ \frac{500GL_i}{231\Omega_{b,i} H_i^2 [1 - \cos(\alpha/2)]} \right\}^{1/5}. \quad (\text{A6})$$

Most terms in equations (A1) and (A2) diverge at  $t = 0$ . To obtain a system of first order equations that is well-behaved at  $t = 0$ , we introduce the following transformations,

$$S = Rt^{2/5}, \quad (\text{A7})$$

$$q = pt^{9/5}, \quad (\text{A8})$$

$$U = \dot{S}t. \quad (\text{A9})$$

Equations (A1), (A2), and (A9) reduce to

$$\dot{q} = \frac{19q}{5t} + \frac{Lt^3}{2\pi[1 - \cos(\alpha/2)]S^3} - \frac{5qU}{St}, \quad (\text{A10})$$

$$\dot{S} = \frac{U}{t}, \quad (\text{A11})$$

$$\begin{aligned} \dot{U} = & \frac{9U}{5t} - \frac{14S}{25t} + \frac{8\pi(q - q_{\text{ext}})G}{\Omega_b H^2 S} - \frac{3t}{S} \left( \frac{U}{t} - \frac{2S}{5t} - HS \right)^2 - \frac{\Omega H^2 St}{2} \\ & - \frac{GMt^{11/5}}{S^2}. \end{aligned} \quad (\text{A12})$$

The 3 quantities  $S$ ,  $q$ , and  $U$  vary linearly with  $t$  at small  $t$ . None of the terms in equations (A10)–(A12) diverges at  $t = 0$ . These equations can be integrated numerically using a standard Runge-Kutta algorithm,

with the initial conditions  $S = q = U = 0$  at  $t = 0$ . Before doing so, it is preferable to rewrite the equations in dimensionless form. We define

$$\tau \equiv H_0 t, \quad (A13)$$

$$\tilde{S} \equiv H_0 S/C, \quad (A14)$$

$$\tilde{U} \equiv H_0 U/C, \quad (A15)$$

$$\tilde{q} \equiv Gq/H_0 C^2, \quad (A16)$$

$$f_H \equiv H/H_0, \quad (A17)$$

$$f_L \equiv L/L_i, \quad (A18)$$

$$\mathcal{M} \equiv GM/C^3 H_0^{1/5}. \quad (A19)$$

Equations (A10)–(A12) reduce to their dimensionless form

$$\frac{d\tilde{q}}{d\tau} = \frac{19\tilde{q}}{5\tau} + \frac{231\Omega_{b,i}f_L f_{H,i}^2 \tau^3}{1000\pi \tilde{S}^3} - \frac{5\tilde{q}\tilde{U}}{\tilde{S}\tau}, \quad (A20)$$

$$\frac{d\tilde{S}}{d\tau} = \frac{\tilde{U}}{\tau}, \quad (A21)$$

$$\begin{aligned} \frac{d\tilde{U}}{d\tau} = & \frac{9\tilde{U}}{5\tau} - \frac{14\tilde{S}}{25\tau} + \frac{8\pi(\tilde{q} - \tilde{q}_{\text{ext}})}{\Omega_{b,i} f_{H,i}^2 \tilde{S}} - \frac{3\tau}{\tilde{S}} \left( \frac{\tilde{U}}{\tau} - \frac{2\tilde{S}}{5\tau} - f_H \tilde{S} \right)^2 - \frac{\Omega f_{H,i}^2 \tilde{S} \tau}{2} \\ & - \frac{\mathcal{M} \tau^{11/5}}{\tilde{S}^2}, \end{aligned} \quad (A22)$$

where  $f_{H,i} = H_i/H_0$ . Interestingly, the change of variable eliminates the explicit dependence upon the opening angle in equation (A20).

The quantity  $f_L$  appearing in equation (A20) depends on the luminosity  $L_{\text{comp}}$ , which is given by equation (16). We eliminate  $p$  and  $R$  in equation (16), using equations (A7), (A8), (A13), (A14), and (A16), then eliminate  $C$  using equation (A6). We get

$$\frac{L_{\text{comp}}}{L_i} = \frac{200\pi^3}{2079} \frac{\sigma_t \hbar}{m_e H_0 \Omega_{b,i} f_{H,i}^2} \left( \frac{kT_{\gamma 0}}{\hbar c} \right)^4 \left( 1 - \cos \frac{\alpha}{2} \right) (1+z)^4 \frac{\tilde{q} \tilde{S}^3}{\tau^3}. \quad (A23)$$

The initial conditions are  $\tilde{S} = \tilde{q} = \tilde{U} = 0$  at  $\tau = 0$ . In the limit  $\tau \rightarrow 0$ , the derivatives reduce to  $d\tilde{S}/d\tau = d\tilde{U}/d\tau = 1$ , and  $d\tilde{q}/d\tau = 21\Omega_{b,i} f_{H,i}^2 / 200\pi$ .

## REFERENCES

- Aguirre, A., Hernquist, L., Schaye, J., Katz, N. , Weinberg, D. H., & Gardner, J. 2001, ApJ, 561, 521
- Bennett, C. L. et al. 2003, ApJS, 148, 1
- Bi, H., & Davidsen, A. F., 1997, ApJ, 479, 523
- Bland, L., & Tully, R. B. 1988, Nature, 334, 43
- Brook, C. B., Gibson, B. K., Martel, H., & Kawata, D. 2005, ApJ, 630, 298
- Brook, C. B., Richard, S., Martel, H., Kawata, D., & Gibson, B. K. 2005, in preparation
- Carignan, C., Beaulieu, S., Côté, S., Demers, S., & Mateo, M. 1998, AJ, 116, 1690
- Choudhury, T. R., & Ferrara, A. 2005, MNRAS, 361, 577
- Choudhury, T. R., & Ferrara, A. 2006, submitted (astro-ph/0603617)
- Davis, M., Efstathiou, G., Frenk, C. S., & White, S. D. M. 1985, ApJ, 292, 371
- Eke, V. R., Cole, S., & Frenk, C. S. 1996, MNRAS, 282, 263
- Fabbiano, G., Heckman, T., Keel, W. C. 1990, ApJ, 355, 442
- Heckman, T. M., Lehnert, M. D., Strickland, D. K., & Armus, L. 2000, ApJS, 129, 493
- Hockney, R. W., & Eastwood, J. W. 1981, *Computer Simulation using Particles* (New York: McGraw Hill).
- Hui, L., & Gnedin, N. Y. 1997, MNRAS, 292, 27
- Izotov, Y. I., & Thuan, T. X. 2004, ApJ, 602, 200
- Kroupa, P. 2001, MNRAS, 322, 231
- Leitherer, C., & Heckman, T. M. 1995, ApJ, 96, 9
- Mac Low, M.-M., & Ferrara, A. 1999, ApJ, 513, 142
- Madau, P., Ferrara, A., & Rees, M. J. 2001, ApJ, 555, 92
- Martel, H. 1991, ApJ, 377, 7
- Martel, H. 2005, Technical Report UL-CRC/CTN-RT003 (astro-ph/0506540)
- Martel, H., Grenon, C., & Pieri, M. M. 2006, in preparation.
- Martel, H., & Shapiro, P. R. 2001a, Rev.Mex.A&A (SC), 10, 101
- Martel, H., & Shapiro, P. R. 2001b, in *Relativistic Astrophysics*, AIP Conference Proceedings 586, eds. J. C. Wheeler & H. Martel, p. 265
- Mori, M., Ferrara, A., & Madau, P. 2002, ApJ, 571, 40
- Nagataki, S., & Sato, K. 1998, ApJ, 504, 629

- Navarro, J. F., Frenk, C. S., & White, S. D. M. 1997, *ApJ*, 490, 493
- Norman, M. L., O'Shea, B. W., & Paschos, P. 2004, *ApJ*, 601, L115
- Noh, Y., & Lee, J. 2006, *ApJ*, submitted (astro-ph/0602575)
- Oppenheimer, B. D., & Davé, R. 2006, preprint (astro-ph/0605651)
- Owen, J. M., Villumsen, J. V., Shapiro, P. R., & Martel, H. 1998, *ApJS*, 116, 155
- Pieri, M. M., Grenon, C., & Martel, H. 2006, in preparation.
- Pieri, M. M., & Haehnelt, M. G. 2004, *MNRAS*, 347, 985
- Pieri, M. M., Schaye, J., & Aguirre, A. 2006, *ApJ*, 638, 45
- Press, W. H., & Schechter, P. 1974, *ApJ*, 187, 425
- Scannapieco, E., & Broadhurst, T. 2001, *ApJ*, 549, 28 (SB01)
- Scannapieco, E., Thacker, R. J., & Davis, M. 2001, *ApJ*, 557, 605
- Scannapieco, E., Ferrara, A., & Broadhurst, T. 2000, *ApJ*, 536, L11
- Scannapieco, E., Ferrara, A., & Madau, P. 2002, *ApJ*, 574, 590 (SFM)
- Schaye, J., Aguirre, A., Kim, T., Theuns, T., Rauch, M., & Sargent, W. L. W. 2003, *ApJ*, 596, 768
- Shapiro, P. R., Martel, H., Villumsen, J. V., & Owen, J. M. 1996, *ApJS*, 103, 269
- Shopbell, P. L., & Bland-Hawthorn, J. 1998, *ApJ*, 493, 129
- Sigward, F., Ferrara, A., & Scannapieco, E. 2005, *MNRAS*, 358, 755
- Strickland, D. K., Heckman, T. M., Weaver, K. A., Dahlem, M. 2000, *AJ*, 120, 2965
- Somerville, R. S. 1997, Ph.D. thesis, Univ. California, Santa Cruz
- Springel, V., & Hernquist, L. 2003, *MNRAS*, 312, 334
- Sutherland, R. S., & Dopita, M. A 1993, *ApJS*, 88, 253
- Tegmark, M., Silk, J., & Evrard, A. 1993, *ApJ*, 417, 54 (TSE)
- Theuns, T., Viel, M., Kay, S., Schaye, J., Carswell, R. F., & Tzanavaris, P. 2002, *ApJ*, 578, L5
- Thoul, A., & Weinberg, D. H. 1996, *ApJ*, 465, 608
- Veilleux, S., & Rupke, D. S. 2002, *ApJ*, 565, L63
- White, S. D. M., & Frenk, C. S. 1991, *ApJ*, 379, 52